Linear Frequency Domain and Harmonic Balance Predictions of Dynamic Derivatives

A. Da Ronch [1], A. J. McCracken [2], K. J. Badcock [3]
University of Liverpool, Liverpool, L69 3BX, United Kingdom

M. Widhalm [4]
German Aerospace Center (DLR), Braunschweig, 38108, Germany

M. S. Campobasso [5]
Glasgow University, Glasgow, G12 8QQ, United Kingdom

Dynamic derivatives are used to represent the influence of the aircraft motion rates on the aerodynamic forces and moments needed for studies of flight dynamics. The use of computational fluid dynamics has potential to supplement costly wind tunnel testing. The article considers the problem of the fast computation of forced periodic motions using the Euler equations. Three methods are evaluated. The first is computation in the time-domain which provides the benchmark solution in the sense that the time-accurate solution is obtained. Two acceleration techniques in the frequency-domain are compared. The first uses an harmonic solution of the linearised problem, referred to as the Linear Frequency Domain approach. The second uses the Harmonic Balance method, which approximates the non-linear problem using a number of Fourier modes. These approaches are compared for ability to predict dynamic derivatives and for computational cost. The NACA 0012 aerofoil and the DLR-F12 passenger jet wind tunnel model are the test cases. Compared to time-domain simulations an order of magnitude reduction in CPU costs is achieved, and satisfactory predictions are ob-

[1] Research Associate, School of Engineering; A.Da-Ronch@liverpool.ac.uk. Member AIAA (Corresponding Author).
[2] Ph.D. Student, School of Engineering.
[3] Professor, School of Engineering. Senior Member AIAA.
[4] Research Scientist, Institute of Aerodynamics and Flow Technology; Member AIAA.
[5] Lecturer, School of Engineering.

tained for cases with a narrow frequency spectrum and moderate amplitudes using the frequency-domain methods.

Nomenclature

$\mathbf{A}$ = matrix in frequency domain equation

c = mean aerodynamic chord

C_m = pitching moment coefficient

$C_{m\,0}$ = non-linear static pitching moment coefficient

$\bar{C}_{m_\alpha}$ = in-phase component of pitching moment coefficient

$\bar{C}_{m_q}$ = pitching moment damping coefficient

C_N = normal force coefficient

$C_{N\,0}$ = non-linear static normal force coefficient

$\bar{C}_{N_\alpha}$ = in-phase component of normal force coefficient

$\bar{C}_{N_q}$ = normal force damping coefficient

$\mathbf{D}$ = matrix in harmonic balance equation

$\mathscr{F}\left[\psi(t)\right]$ = Fourier transform of quantity $\psi(t)$; equivalent to $\tilde{\psi}(j\,\omega)$

f = dimensional frequency

j = imaginary unit, $\sqrt{-1}$

k = reduced oscillation frequency, $\omega\, c/2\, U_\infty$

M = freestream Mach number

n_c = number of oscillatory cycles

n_H = number of harmonics

$\mathbf{R}$ = residual vector

$R\left(\omega\right)$ = amplitude ratio of transfer function

s = wing semi-span

t = physical time

t^* = non-dimensional time, $t\, U_\infty/c$

U_∞ = freestream speed

$\mathbf{W}$ = vector of conserved variables

$\angle\tilde{\psi}(j\,\omega)$ = phase angle of the Fourier transform of quantity $\psi(t)$

Greek

α = angle of attack

α_0 = mean angle of attack

α_A = amplitude of oscillatory motion

$\phi\,(\omega)$ = phase angle between output and input

ω = oscillation frequency, $2\,\pi\,f$

Subscript

0 = mean value

A = amplitude

hb = harmonic balance

Superscript

$\widehat{\ }$ = Fourier coefficient

$\widetilde{\ }$ = perturbation amplitude

I. Introduction

For flight dynamics, the aerodynamic model introduced by Bryan [1] is often used. The force and moment dependency on flight and control states is expressed in linear form, with the coefficients referred to as aerodynamic derivatives. There are three types of derivative, static, dynamic and control [2]. Dynamic derivatives are calculated from observing the response of aerodynamic forces and moments to translational and rotational motions. Dynamic derivatives influence the aerodynamic damping of aircraft motions and are used to evaluate the aircraft response and the open-loop stability, e.g., short-period, Phugoid and Dutch roll modes.

There are several possible sources of data for the generation of the aerodynamic model. Flight testing the aircraft is the most realistic but also the most expensive of these methods [3]. Wind-tunnel testing of scaled models is cheaper than flight testing. However, blockage, scaling and Reynolds number effects together with support interference issues limit the proper modelling of the full scale aircraft behaviour [4]. The third approach combines data sheets, linear aerodynamic theory and empirical relations [5]. Due to simplicity, this method is in widespread use and is a common choice to obtain aerodynamic characteristics in the conceptual design stage [6]. In the absence of a background database, empiricism is strongly limited when confronted with novel configurations and flight conditions dominated by non-linear aerodynamic effects.

A possible useful addition to the high-fidelity/high-cost of testing and low-fidelity/low-cost of semi-empirical approaches is Computational Fluid Dynamics (CFD), which represents the state of the art in predicting non-linear flow physics [7]. The computation of static stability derivatives can be done with off-the-shelf CFD tools. However, the generality realized in a CFD simulation comes at the expense of computational cost. The use of high-fidelity CFD simulations to cover a large parameter space of conditions is costly, and, particularly, so when tackling unsteady problems. Extensive computer resources are required for time-domain simulations for the prediction of dynamic derivatives [8]. Recent studies [9–12] demonstrated the desirability to complement and replace engineering methods with CFD.

A common wind-tunnel testing technique for the prediction of dynamic derivatives relies on harmonic forced-oscillation tests. After the decay of initial transients, the nature of the aerodynamic loads becomes periodic. A time-domain simulation of this problem requires significant computational effort. Several oscillatory cycles have to be simulated to obtain a harmonic aerodynamic response, and a time-accurate solution requires a small time-step increment to accurately capture the flow dynamics [13, 14]. Time-domain calculations support a continuum of frequencies up to the frequency limits given by the temporal and spatial resolution, but dynamic derivatives are computed at the frequency of the applied sinusoidal motion. It is therefore worthwhile to consider a frequency-domain formulation to obtain a good estimate of the derivatives at reduced computational cost. The computational methods used in this paper, the Harmonic Balance (HB) and the Linear Frequency

Domain (LFD) methods, provide the ability to efficiently approximate the aerodynamics resulting from small, periodic and unsteady perturbations of the geometry of an aircraft configuration. By resolving only the frequencies of interest, the computational cost of dynamic derivatives is greatly reduced. Initially developed in the field of turbomachinery [15, 16], the HB and LFD methods have been subsequently used for external aerodynamics applied to aircraft problems [17–19]. Murman [20] envisioned the exploitation of the periodicity to reduce the cost of computing dynamic derivatives. The concept of an adaptive HB method has also been put forward, with good success [21, 22]. A large amount of research has been devoted to applications of the HB and the LFD technologies to a broad spectrum of engineering disciplines. There is the question of the influence of the approximations on the derivative predictions. The evaluation of the computational benefits and the predictive limitations are the subject of this study. The contribution of this work is to look at the adequacy of frequency domain methods for the rapid calculation of dynamic derivatives for use in flight dynamics analysis. An extension on previous work to include key flow regimes is also done. This enables a thorough investigation of the dependencies of dynamic derivatives on model parameters to be performed, and to assess the limitations of the tabular aerodynamic models traditionally used by flight dynamicists [23].

The article begins with a description of the time-domain, HB and LFD methods. Results are then presented to compare the dynamic derivative predictions obtained from the time-domain and from the acceleration methods. Two test cases are considered for transonic flows. Conclusions are then given.

II. Numerical Approach

The HB and the LFD methods compared in the current work are implemented in different CFD codes. The approach taken in the results section is to benchmark each against the underlying time-domain flow solver. In the current section the underlying flow solvers are first summarised, and then the HB and LFD methods described.

A. Time-Domain Formulations

1. *University of Liverpool (PMB)*

The main features of the Parallel Multiblock (PMB) solver are described in Badcock et al. [24] A fully implicit steady solution of the Reynolds-Averaged Navier-Stokes (RANS) or Euler equations is obtained by advancing the solution forward in time by solving the discrete non-linear system of equations

$$\frac{\mathbf{W}^{n+1} - \mathbf{W}^{n}}{\Delta\, t^{*}} \;=\; -\,\mathbf{R}\left(\mathbf{W}^{n+1}\right) \tag{1}$$

The term on the right hand side, called the residual, is the discretisation of the convective terms, given here by Osher's approximate Riemann solver [25], MUSCL interpolation [26] and Van Albada's limiter. Equation (1) is a non-linear system of algebraic equations which is solved by an implicit method [24], the main features of which are an approximate linearisation to reduce the number of non-zero matrix entries and the condition number of the linear system, and the use of a preconditioned Krylov subspace method to calculate the updates.

The steady state solver is applied to unsteady problems within a pseudo time stepping iteration [27] which at each real time step is written as

$$\left[\left(\frac{1}{\Delta t^{*}} - \frac{3}{2\Delta\, t}\right)\mathbf{I} + \frac{\partial \mathbf{R}}{\partial \mathbf{W}}\right]\Delta\mathbf{W} = -\left(\mathbf{R}(\mathbf{W}) + \frac{3\mathbf{W}^{n+1} - 4\mathbf{W}^{n} + \mathbf{W}^{n-1}}{2\Delta t}\right) \tag{2}$$

where Δt is the real time step. Periodicity can be used to approximate the initial solution for the pseudo time stepping at each real time step. At each iteration a file is written to the local disk with the converged solution at that real time step. On the next cycle this file is read to provide the initial solution for the pseudo time stepping, and on convergence to the next real time solution, the original file is overwritten with the updated solution. As the solution approaches a periodic state the pseudo time stepping converges quickly because it starts from an excellent initial guess. In this way results can be obtained from time marching in a very efficient manner.

2. *German Aerospace Center (TAU)*

The DLR TAU code [28, 29] is a modern massively parallel software system for the simulation of flows around complex geometries from low subsonic to hypersonic flow regimes. The different

modules of TAU can be used stand-alone or in a more efficient way within a Python scripting framework which allows for inter-module communication without file I/O by using common memory allocations. The unsteady compressible RANS flow solver is based on hybrid unstructured grids with a finite volume discretization. The flow solver uses an edge-based dual-cell approach, either cell-vertex or cell-centred, employing either a second-order central scheme or a variety of upwind schemes with linear reconstruction for second order accuracy.

As for the PMB solver, unsteady simulations use Jameson's dual-time-stepping method [27] to integrate the equations in the time-domain. Additionally, the solver respects the geometric conservation law, and bodies which are deforming and in arbitrary motion can be simulated. For the pseudo time stepping various explicit Runge-Kutta and a semi-implicit Lower-Upper Symmetric Gauss-Seidel (LU-SGS) scheme are available for enhancing convergence acceleration with a geometrical multi-grid algorithm and local time-stepping.

TAU includes an adjoint-solver for gradient based numerical shape optimization. The discrete adjoint method [30] consists of the explicit construction of the exact flux Jacobians of the spatial discretization with respect to the unknown flow variables allowing the adjoint equations to be formulated and solved, and is an important part of the linear frequency domain solver and error estimation methods.

3. University of Glasgow (COSA)

The structured multi-block Navier-Stokes solver COSA is an explicit multigrid finite volume cell-centered code. It solves the integral conservation laws in generalized curvilinear coordinates making use of a second order discretisation method. The discretisation of the convective fluxes is based on Van Leer's MUSCL extrapolations and the approximate Riemann solver of Roe's flux difference splitting. The discretisation of the viscous fluxes uses centered finite differences. The set of nonlinear algebraic equations resulting from the spatial discretisation of the conservation laws is solved with an explicit approach based on the use of a four-stage Runge-Kutta smoother. The convergence rate is greatly enhanced by means of local time-stepping, variable-coefficient central implicit residual smoothing and a full approximation storage multigrid algorithm. When solving problems at very

low flow speed, computational accuracy and high rates of convergence are maintained by using a carefully designed low-speed preconditioner [31].

In the case of unsteady problems, Jameson's dual-time-stepping method [27] is used to integrate the equations in the time-domain. The interested reader is referred to references [31–33] for further details on the COSA solver and a thorough validation of its inviscid and viscous capabilities for steady and unsteady problems.

B. Frequency-Domain Methods

1. Harmonic Balance Method

As an alternative to time marching, the Harmonic Balance method [34] allows for a direct calculation of the periodic state. Write the semi-discrete form as a system of ordinary differential equations

$$\mathbf{I}(t) = \frac{d\mathbf{W}(t)}{dt} + \mathbf{R}(t) = 0 \tag{3}$$

Consider the solution vector $\mathbf{W}$ and residual $\mathbf{R}$ to be periodic in time and a function of ω,

$$\mathbf{W}(t) \approx \widehat{\mathbf{W}}_0 + \sum_{n=1}^{N_H} \left(\widehat{\mathbf{W}}_{a_n} \cos(\omega n t) + \widehat{\mathbf{W}}_{b_n} \sin(\omega n t) \right) \tag{4}$$

$$\mathbf{R}(t) \approx \widehat{\mathbf{R}}_0 + \sum_{n=1}^{N_H} \left(\widehat{\mathbf{R}}_{a_n} \cos(\omega n t) + \widehat{\mathbf{R}}_{b_n} \sin(\omega n t) \right) \tag{5}$$

giving a system of $N_T = 2N_H + 1$ equations in N_T unknown harmonic terms, which can be expressed as

$$\omega \mathbf{A} \widehat{\mathbf{W}} + \widehat{\mathbf{R}} = 0 \tag{6}$$

where $\mathbf{A}$ is a $N_T \times N_T$ matrix containing the entries $\mathbf{A}(n+1, N_H+n+1) = n$ and $\mathbf{A}(N_H+n+1, n+1) = -n$, and $\widehat{\mathbf{W}}$ and $\widehat{\mathbf{R}}$ are vectors of the Fourier coefficients.

The difficulty with solving Eq. (6) is in finding a relationship between $\widehat{\mathbf{R}}$ and $\widehat{\mathbf{W}}$. To avoid this problem, the system is converted back to the time domain. The solution is split into N_T discrete

equally spaced sub-intervals over the period $T = 2\pi/\omega$

$$\mathbf{W}_{hb} = \begin{Bmatrix} \mathbf{W}(t_0 + \Delta t) \\ \mathbf{W}(t_0 + 2\Delta t) \\ \vdots \\ \mathbf{W}(t_0 + T) \end{Bmatrix} \qquad \mathbf{R}_{hb} = \begin{Bmatrix} \mathbf{R}(t_0 + \Delta t) \\ \mathbf{R}(t_0 + 2\Delta t) \\ \vdots \\ \mathbf{R}(t_0 + T) \end{Bmatrix} \tag{7}$$

where $\Delta t = 2\pi/(N_T\omega)$. **Then there is a transformation matrix E (see Eq. 19) such that**

$$\mathbf{W}_{hb} \,=\, \mathbf{E}^{-1}\,\widehat{\mathbf{W}}, \qquad \mathbf{R}_{hb} \,=\, \mathbf{E}^{-1}\,\widehat{\mathbf{R}} \tag{8}$$

and combining with Eq. (6) gives

$$\begin{aligned} &\omega\,\mathbf{A}\,\mathbf{E}\,\mathbf{W}_{hb} \,+\, \mathbf{E}\,\mathbf{R}_{hb} \,=\, 0 \\ &\omega\,\mathbf{E}^{-1}\,\mathbf{A}\,\mathbf{E}\,\mathbf{W}_{hb} \,+\, \mathbf{E}^{-1}\,\mathbf{E}\,\mathbf{R}_{hb} \,=\, 0 \\ &\omega\,\mathbf{D}\,\mathbf{W}_{hb} \,+\, \mathbf{R}_{hb} \,=\, 0 \end{aligned} \tag{9}$$

where the components of $\mathbf{D}$ are defined by

$$D_{i,j} = \frac{2}{N_T}\sum_{k=1}^{N_H} k\sin(2\pi k(j-i)/N_T) \tag{10}$$

One can then apply pseudo-time marching to the harmonic balance equation

$$\frac{d\mathbf{W}_{hb}}{dt} + \omega\,\mathbf{D}\,\mathbf{W}_{hb} + \mathbf{R}_{hb} = 0 \tag{11}$$

The HB method was implemented within the structured PMB and COSA codes. The main difference between the PMB and COSA implementations is that the former solves the equations with an implicit method [35], whereas the latter adopts an explicit multigrid integration [36]. Reference [36] presents a stabilization technique to handle the harmonic balance source term, $\omega\,\mathbf{D}\,\mathbf{W}_{hb}$, when using an explicit numerical integration process. Such a stabilization method can be viewed as the counterpart of that reported in reference [37], which instead applies to the case of implicit integration. The parallelization of the COSA explicit multigrid HB solver is based on a hybrid distributed (MPI) and shared (OpenMP) architecture, which is reported in reference [38].

2. Linear Frequency Domain Method

The Linear Frequency Domain (LFD) method [39] is obtained by linearizing Eq. (6), in which the residual $\widehat{\mathbf{R}}$ is considered as a function of the grid point locations, $\mathbf{x}$, the grid point velocities, $\dot{\mathbf{x}}$, and flow solution, $\mathbf{W}$. Assuming an unsteady motion with a small amplitude, the unsteady terms can be expressed as a superposition of a steady mean state and a perturbation, which is expressed by a Fourier series

$$\begin{aligned}
&\mathbf{W}(t) \approx \widehat{\mathbf{W}}_0 + \widetilde{\mathbf{W}}(t), && \|\widetilde{\mathbf{W}}\| \ll \|\widehat{\mathbf{W}}_0\| \\
&\mathbf{x}(t) \approx \widehat{\mathbf{x}}_0 + \widetilde{\mathbf{x}}(t), && \|\widetilde{\mathbf{x}}\| \ll \|\widehat{\mathbf{x}}_0\| \\
&\dot{\mathbf{x}}(t) \approx \dot{\widetilde{\mathbf{x}}}(t)
\end{aligned}$$

When linearizing about the steady mean state, Eq. (6) results in the following complex-valued linear system of equations for the n-th mode index

$$\begin{bmatrix} \partial\mathbf{R}/\partial\mathbf{W} & \omega\, n\, \mathbf{I} \\ -\omega\, n\, \mathbf{I} & \partial\mathbf{R}/\partial\mathbf{W} \end{bmatrix} \begin{Bmatrix} \widehat{\mathbf{W}}_{a_n} \\ \widehat{\mathbf{W}}_{b_n} \end{Bmatrix} = - \begin{bmatrix} \partial\mathbf{R}/\partial\mathbf{x} & \omega\, n\, \partial\mathbf{R}/\partial\dot{\mathbf{x}} \\ -\omega\, n\, \partial\mathbf{R}/\partial\dot{\mathbf{x}} & \partial\mathbf{R}/\partial\mathbf{x} \end{bmatrix} \begin{Bmatrix} \widehat{\mathbf{X}}_{a_n} \\ \widehat{\mathbf{X}}_{b_n} \end{Bmatrix} \tag{12}$$

Derivatives of the residual are all evaluated at the steady mean state $(\widehat{\mathbf{W}}_0, \widehat{\mathbf{x}}_0)$. This system of equations can be written in the form of a linear equation, $\mathbf{A}\,\mathbf{x} = \mathbf{b}$.

The Jacobian $\partial\mathbf{R}/\partial\mathbf{W}$ has been obtained previously in the context of the discrete adjoint method by analytic differentiation of the flow solver. Considerable attention has been given to ensure that the evaluation of the Jacobian and matrix-vector products involving the Jacobian are efficient in terms of memory and time, and require no more than four times the memory requirement of the non-linear code. The frequency domain residual requires two products of a vector with the Jacobian, and hence a single evaluation is approximately 20 to 60% more expensive than a non-linear residual evaluation on the same case.

The terms $\partial\mathbf{R}/\partial\mathbf{x}$ and $\partial\mathbf{R}/\partial\dot{\mathbf{x}}$, which arise from the prescribed periodic deformation of the grid, are evaluated using central finite differences

$$\frac{\partial\mathbf{R}}{\partial\mathbf{x}}\,\widetilde{\mathbf{x}} \;\approx\; \frac{\mathbf{R}\left(\widehat{\mathbf{W}}_0\,,\,\widehat{\mathbf{x}}_0 + \epsilon\,\widetilde{\mathbf{x}}\,,\,0\right) - \mathbf{R}\left(\widehat{\mathbf{W}}_0\,,\,\widehat{\mathbf{x}}_0 - \epsilon\,\widetilde{\mathbf{x}}\,,\,0\right)}{2\,\epsilon} \tag{13}$$

$$\frac{\partial\mathbf{R}}{\partial\dot{\mathbf{x}}}\,\dot{\widetilde{\mathbf{x}}} \;\approx\; \frac{\mathbf{R}\left(\widehat{\mathbf{W}}_0\,,\,\widehat{\mathbf{x}}_0\,,\,\epsilon\,\dot{\widetilde{\mathbf{x}}}\right) - \mathbf{R}\left(\widehat{\mathbf{W}}_0\,,\,\widehat{\mathbf{x}}_0\,,\,-\epsilon\,\dot{\widetilde{\mathbf{x}}}\right)}{2\,\epsilon} \tag{14}$$

where ϵ is a small number chosen to balance truncation and rounding errors.

C. Method of Data Analysis

Modeling the aircraft aerodynamics for studies of flight dynamics commonly assumes that the aerodynamic loads depend only on the instantaneous values of the motion variables, and vary linearly with these variables. Based on this formulation, small amplitude oscillatory tests are used to estimate the dynamic derivatives. To illustrate, a forced sinusoidal motion around the pitch axis defines the angle of attack as a function of time

$$\alpha \;=\; \alpha_0 \;+\; \alpha_A \,\sin\left(\omega\, t\right) \tag{15}$$

It is also convenient to introduce the non-dimensional reduced frequency of the applied motion, $k = \omega\, c/(2\, U_\infty)$, based on the mean aerodynamic chord and freestream speed. Within the linearity assumption, the aerodynamic loads are harmonic at the same frequency of the forced motion and with a phase lag with respect to the motion variables. The dynamic derivatives are then obtained from the time histories of the loads over n_c oscillatory cycles [13]

$$\bar{C}_{i_\alpha} \equiv C_{i_\alpha} - k^2\, C_{i_{\dot{q}}} \;=\; \frac{2}{\alpha_A\, n_c\, T} \int_0^{n_c\, T} \Delta\, C_i\,(t)\, \sin\left(\omega\, t\right)\, dt \tag{16}$$

$$\bar{C}_{i_q} \equiv C_{i_{\dot{\alpha}}} + C_{i_q} \;=\; \frac{2}{k\, \alpha_A\, n_c\, T} \int_0^{n_c\, T} \Delta\, C_i\,(t)\, \cos\left(\omega\, t\right)\, dt \tag{17}$$

$$\text{for } \; i = L, D, \;\; \text{and } \; m$$

where $\Delta\, C_i$ represents the increment in the longitudinal aerodynamic coefficients with respect to the mean value during the applied pitching sinusoidal motion. In conventional oscillatory tests, only composite derivatives, which include a combination of the pure rotation (due to q) and vertical acceleration effect (due to $\dot{\alpha}$), can be measured. The effects of the angle of attack change and the pitching rate can be separated by performing heave oscillations. In this case, the variations of the aerodynamic loads are caused by pure angle of attack change, and estimations of the $C_{i_{\dot{\alpha}}}$ are obtained. Note that in Eq. (16), the static derivative C_{i_α} can be computed from a set of steady-state runs.

The numerical integration of Eqs. (16) and (17) can be achieved using quadrature methods. An alternative approach is based on the solution of a least squares problem. Further details on these techniques can be found, for example, in Da Ronch et al. [13] A post-processing utility was

implemented for the extraction of the zeroth and first harmonic flow solution computed from time-domain solutions. This was also used for the results presented using the LFD solver.

A different approach was adopted for the HB solver, whose solution is computed at $N_T = 2\,N_H + 1$ equally spaced points in time over one cycle. Then

$$\mathbf{W}\,(x,\,y,\,z,\,t) \approx \widehat{\mathbf{W}}_0\,(x,\,y,\,z) + \sum_{n=1}^{N_H} \left(\widehat{\mathbf{W}}_{a_n}\,(x,\,y,\,z)\,\cos\left(\omega\,n\,t\right) + \widehat{\mathbf{W}}_{b_n}\,(x,\,y,\,z)\,\sin\left(\omega\,n\,t\right)\right) \quad (18)$$

where $\widehat{\mathbf{W}}_0$, $\widehat{\mathbf{W}}_{a_n}$ and $\widehat{\mathbf{W}}_{b_n}$ are the Fourier coefficients of a flow variable, $\mathbf{W}\,(x,\,y,\,z,\,t)$. This expression is easily re-written in matrix form as

$$\underbrace{\begin{Bmatrix} \mathbf{W}_1 \\ \mathbf{W}_2 \\ \vdots \\ \mathbf{W}_{N_T} \end{Bmatrix}}_{\mathbf{W}_{hb}} = \underbrace{\begin{bmatrix} 1 & \cos\left(\omega\,t_1\right) & \sin\left(\omega\,t_1\right) & \dots & \cos\left(N_H\,\omega\,t_1\right) & \sin\left(N_H\,\omega\,t_1\right) \\ 1 & \cos\left(\omega\,t_2\right) & \sin\left(\omega\,t_2\right) & \dots & \cos\left(N_H\,\omega\,t_2\right) & \sin\left(N_H\,\omega\,t_2\right) \\ \vdots & \vdots & \vdots & \ddots & \vdots & \vdots \\ 1 & \cos\left(\omega\,t_{N_T}\right) & \sin\left(\omega\,t_{N_T}\right) & \dots & \cos\left(N_H\,\omega\,t_{N_T}\right) & \sin\left(N_H\,\omega\,t_{N_T}\right) \end{bmatrix}}_{\mathbf{E}^{-1}} \underbrace{\begin{Bmatrix} \widehat{\mathbf{W}}_0 \\ \widehat{\mathbf{W}}_{a_1} \\ \widehat{\mathbf{W}}_{b_1} \\ \vdots \\ \widehat{\mathbf{W}}_{a_{N_H}} \\ \widehat{\mathbf{W}}_{b_{N_H}} \end{Bmatrix}}_{\widehat{\mathbf{W}}} \quad (19)$$

where $\mathbf{W}_{hb}$ is the vector of the flow variable at $2\,N_H + 1$ equally spaced points in time over one period, $\mathbf{W}_l = \mathbf{W}(t_0 + l\Delta t)$, and $\mathbf{E}^{-1}$ is the matrix that is the inverse discrete Fourier transform operator. The time instances at which the HB solution is known are denoted by $t_i = t_0 + i\,\Delta\,t$, $i = 1, 2, \dots, N_T$. The Fourier coefficients of the flow variable are computed as $\widehat{\mathbf{W}} = \mathbf{E}\,\mathbf{W}_{hb}$. Dynamic derivatives, as well as the real and imaginary parts of the flow variable, are determined directly from the Fourier coefficients without any additional transformation in the time domain.

Finally, it is worth noting that to determine the stability behaviour of the free-to-pitch oscillations, the work done by the fluid on the airframe over one single period can be formulated as

$$\begin{aligned} E &= \int_{\alpha(0)}^{\alpha(T)} \Delta\,C_m\,(\alpha)\;d\alpha \\ &= \alpha_A\,\omega \int_{t_0}^{t_0+T} \left(\widehat{C}_{m\,a_1}\,\cos\left(\omega\,t\right) + \widehat{C}_{m\,b_1}\,\sin\left(\omega\,t\right)\right)\,\cos\left(\omega\,t\right)\;dt \\ &= 2\,\pi\,\alpha_A\,\widehat{C}_{m\,a_1} \end{aligned} \quad (20)$$

Table 1 Description of the AGARD CT5 conditions for the NACA 0012 aerofoil [40]

Parameter	Value
M	0.755
α_0	0.016 deg
α_A	2.51 deg
k	0.0814

A Fourier series expansion for the pitching moment coefficient, $\Delta C_m(t) = \widehat{C}_{m\,a_1} \cos(\omega t) + \widehat{C}_{m\,b_1} \sin(\omega t)$, was used and the orthogonality of the trigonometric functions (for example, $\int_0^a \cos\left(\frac{\pi x}{a}\right) \cos\left(\frac{\pi x}{a}\right) dx = \frac{a}{2}$) was used to simplify the integral expression above. The result in Eq. (20) shows that the work done by the fluid is proportional to the real part of the aerodynamic moment, $\widehat{C}_{m\,a_1}$. Observing further that Eq. (17) is similar to calculating the cosine term of a Fourier series, it is apparent how the damping term, $\bar{C}_{m_q}$, is proportional to the real part of the aerodynamic moment coefficient, $\widehat{C}_{m\,a_1}$. Hence, for $\alpha_A > 0$, the free pitching oscillation is classified as unstable if $\widehat{C}_{m\,a_1} > 0$ (equivalently, $\bar{C}_{m_q} > 0$), or stable if $\widehat{C}_{m\,a_1} < 0$ (equivalently, $\bar{C}_{m_q} < 0$).

III. Two-Dimensional Case

Experimental data for the NACA 0012 aerofoil undergoing oscillatory pitch motions are available [40]. Measured quantities include the pressure at 30 locations distributed on the aerofoil surface. These data were collected at several time intervals. No transition tripping was applied in the experiments, and corrections corresponding to a steady interference have been applied to the measured quantities. There were some questions about unsteady interference effects on the experimental data. However, the deviation between numerical and experimental data is not the emphasis of the present work which is instead on the quality of the HB and LFD results compared to the time-domain predictions.

This paper focuses on the AGARD CT5 case because it is transonic with strong non-linearities in the aerodynamic loops arising from shock wave motions. The flow conditions for the case CT5 are summarized in Table 1.

Table 2 NACA 0012: grid influence on static and dynamic derivatives obtained from the time-domain PMB solution for the AGARD CT5 conditions

	$C_{N\,0}$	$\bar{C}_{N_\alpha}$	$\bar{C}_{N_q}$	$C_{m\,0}$	$\bar{C}_{m_\alpha}$	$\bar{C}_{m_q}$
Coarse	$3.51\cdot 10^{-3}$	7.66	$-3.71\cdot 10^{1}$	$-7.58\cdot 10^{-5}$	$-1.10\cdot 10^{-1}$	-3.07
Medium	$3.51\cdot 10^{-3}$	7.66	$-3.72\cdot 10^{1}$	$-6.98\cdot 10^{-5}$	$-1.03\cdot 10^{-1}$	-3.14
Fine	$3.51\cdot 10^{-3}$	7.66	$-3.72\cdot 10^{1}$	$-7.15\cdot 10^{-5}$	$-1.03\cdot 10^{-1}$	-3.14

A. Numerical Setup

A preliminary study was made to test that solutions presented are independent of the grid used. Three sets of grids were generated. The two-dimensional domain extends fifty chords from the solid wall to the farfield. A coarsest grid had a total number of 13068 points, with 132 nodes on the aerofoil, and 36 in the normal direction. The wake behind the aerofoil was discretized using 36 points in the streamwise direction. A medium grid consisted of 32028 grid points, 212 nodes were distributed on the aerofoil, 51 points were used in the normal direction and along the streamwise direction for the wake. The finest grid was obtained with a total of 37180 grid points. The structured grids consisted of six blocks, and were converted to an unstructured format for use with the unstructured solver TAU.

Note that the three grids were used in combination with each time-domain solver, and numerical results were compared with tunnel measurements under static [41] and unsteady conditions. Table 2 conveys the grid influence on the dynamic derivatives of the normal force and moment coefficients. Aerodynamic data of the force coefficient show little sensitivity to the grid used. Values of $C_{m\,0}$ can be considered numerically nil and thus grid invariant. For the computations on the medium grid, dynamic derivatives of the moment coefficient are observed to be identical to the respective values obtained using the finest grid. Some deviations are identified in the case of the coarsest grid. Based on this comparison, results presented hereafter are for the medium grid.

Unsteady simulations were run for three periods using 128 time-steps per cycle. A time-step study was also performed for the unsteady PMB solver, and details are given in Sec. III D. The choice of the numerical parameters led to well converged solutions in all cases. For TAU, the CFL number used was 1.5 in combination with a "4w" multigrid cycle. For the LFD, the LU-SGS scheme with

multigrid was used. The COSA pair used three multigrid levels, performing 10 smoothed Runge-Kutta cycles on the coarsest level, and 3 on the finest levels. The CFL number was 4 for both the time-domain and the harmonic balance solver. The implicit CFL number for the PMB solver was 500. A Block Incomplete Lower Upper (BILU) factorization was used with no fill-in for the linear solver preconditioner.

B. Validation

The Euler solutions presented are for the medium grid, shown in Fig. 1. The flow for the AGARD CT5 conditions is non-linear, with a shock appearing in the leading edge region and moving downstream for increasing angle of attack. The shock continues downstream until approximately forty-five per cent of the chord. Then the shock returns upstream close to the leading edge. The same pattern is repeated on the opposite side of the aerofoil. The flow remains attached throughout the cycle of unsteadiness. Since this case features a strong shock on the upper and lower surface, the question is whether the presence of the dynamic shock has a negative impact on the accuracy of the frequency-domain solvers. First, a validation study of the unsteady time-accurate solutions was performed before attempting to compare the spectral methods to the underlying CFD solvers. Figure 2 illustrates the comparison of numerical predictions of integrated aerodynamic loads with experimental data. The initial transient was removed from the numerical solutions, and two arrows indicate the time evolution. If the arrows are oriented in the counter-clockwise direction, the contribution from the dynamic derivative is negative, and vice versa. Results compare well for all time-accurate solutions. It is seen that the force coefficient is harmonic with a phase lag with respect to the forced motion. No contribution from higher harmonics can be detected. The moment coefficient is influenced by the instantaneous location of the moving shock wave due to its moment arm with respect to the reference point. A favourable agreement between the tunnel measurements and the numerical solutions is observed.

Measurements of the instantaneous pressure coefficient distribution were taken at several time instances in one cycle of unsteadiness, and the nearest angle at which numerical results were computed was used for comparison. Numerical solutions are compared with tunnel measurements in

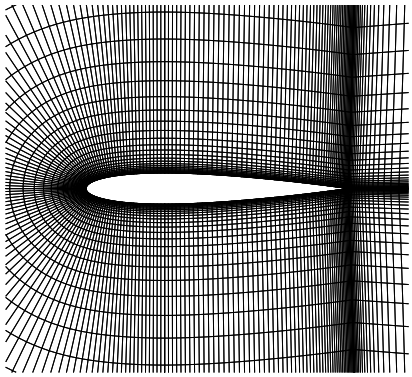

Fig. 1 Medium grid used for the NACA 0012 aerofoil (212×51)

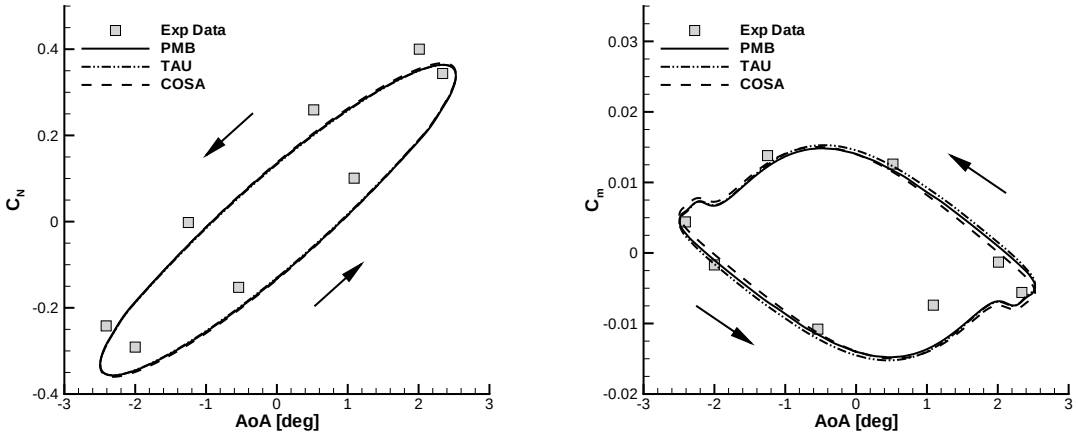

(a) Normal force coefficient

(b) Pitching moment coefficient

Fig. 2 NACA 0012: predictions of unsteady time-accurate Euler solutions ($M = 0.755$**,** $\alpha_0 = 0.016$ **deg,** $\alpha_A = 2.51$ **deg, and** $k = 0.0814$**); experimental data from Landon [40]**

Fig. 3. The numerical solutions agree well with each other, with minor deviations around the shock wave. The overall performance and systematic variations from measurements are in line with other independent numerical investigations, e.g., Batina [42] and Marques et al. [43].

For the range of test cases computed in Da Ronch et al. [13], the dependence of dynamic derivatives on motion and flow conditions was reported. In the present study, the influence of the amplitude of the forced-motion, α_A, was examined for the conditions given in Table 1. Values of amplitude presented are between 0.01 deg and 2.81 deg. The variation of the pitching moment

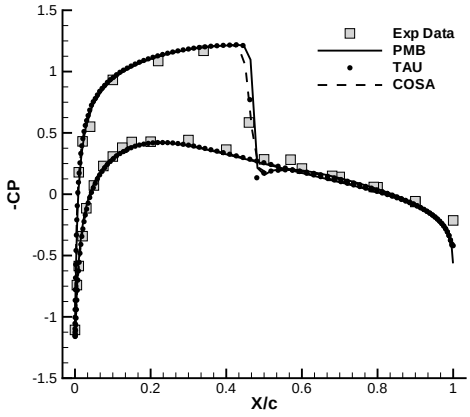

Fig. 3 NACA 0012: instantaneous pressure coefficient distribution at $\alpha = -2.00$ deg for increasing angle compared to experimental data of Landon [40]

coefficient dynamic derivatives is shown in Fig. 4. Dynamic derivatives are nearly constant for small values of oscillatory amplitude, and exhibit a significant variation for values of amplitude larger than approximately 1.0 deg. Predictions obtained using the LFD solver are included in the figure as a dotted line, and are closer to the results obtained using time-domain calculations for small amplitude values. The agreement of the LFD solution with time-domain data is considered adequate for small amplitude values, with an error in the prediction of few percentage points. Increasing the oscillatory amplitude of the forced-motion above approximately 1.0 deg causes the periodic appearance and disappearance of the shock wave on the aerofoil surface, with a considerable impact on dynamic derivatives. Note that dynamic derivatives computed at the nominal conditions of the AGARD CT5 are also included in the figure.

C. Frequency-Domain Results

To demonstrate the convergence of the HB method to the unsteady solution, cases were run using up to 7 harmonics. Figure 5 shows the loops of the integrated loads against the instantaneous angle of attack. The time evolution in the force coefficient was observed to be linear and harmonic with the forced variation in the motion variable. This reflects the satisfactory agreement achieved by the frequency-domain methods using one Fourier harmonic, as illustrated in Fig. 5(a). It also suggests that the motion of the shock wave is harmonic and lags behind the angle of attack change.

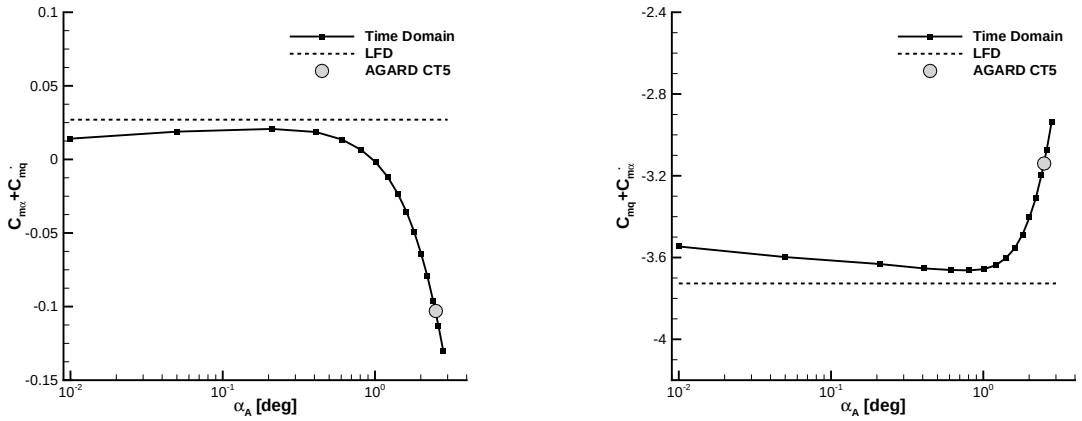

(a) In-phase component, $\bar{C}_{m_\alpha}$

(b) Out-of-phase component, $\bar{C}_{m_q}$

Fig. 4 NACA 0012: influence of amplitude of oscillatory motion, α_A, on the pitching moment coefficient dynamic derivatives ($M = 0.755$, $\alpha_0 = 0.016$ deg, and $k = 0.0814$)

Increasing the number of Fourier modes in the HB solution had little effect on the result, as most of the energy is at the frequency of the applied motion. The moment coefficient is illustrated in the remaining figures for each solver pair, separately. Comparing the harmonic balance solutions obtained using the PMB-HB and COSA-HB highlights the similarity in the results from the two solvers, as shown in Figs. 5(b) and 5(c). Observe that including the third Fourier mode in the HB solution has a far larger impact on improving the correlation to the reference solution than adding the second mode. This reflects the frequency spectrum of the moment coefficient, due to the flow conditions and symmetry in the aerofoil geometry, as described below. Higher modes are not included, but they closely overlap the reference solution. The LFD solution is illustrated in Fig. 5(d), and indicates a degraded prediction of the moment dynamic dependence. Consistent with the other data, the LFD predicts a large hysteresis but the loop is rotated in the opposite direction. This is quantified calculating the system response between the prescribed angle of attack and the aerodynamic loads. Let us denote x and y, respectively, the input and the output of interest. Then, the system response is

$$G\left(j\,\omega\right) \;=\; \frac{\mathscr{F}\left[y\left(t\right)\right]}{\mathscr{F}\left[x\left(t\right)\right]} \;=\; R\left(\omega\right)\, e^{j\,\phi(\omega)} \tag{21}$$

where $R(\omega)$ and $\phi(\omega)$ indicate, respectively, the amplitude ratio and the phase lag, and are defined as

$$R(\omega) = \frac{\|\tilde{y}(j\,\omega)\|}{\|\tilde{x}(j\,\omega)\|} \tag{22}$$

$$\phi(\omega) = \angle\,\tilde{y}(j\,\omega) - \angle\,\tilde{x}(j\,\omega) \tag{23}$$

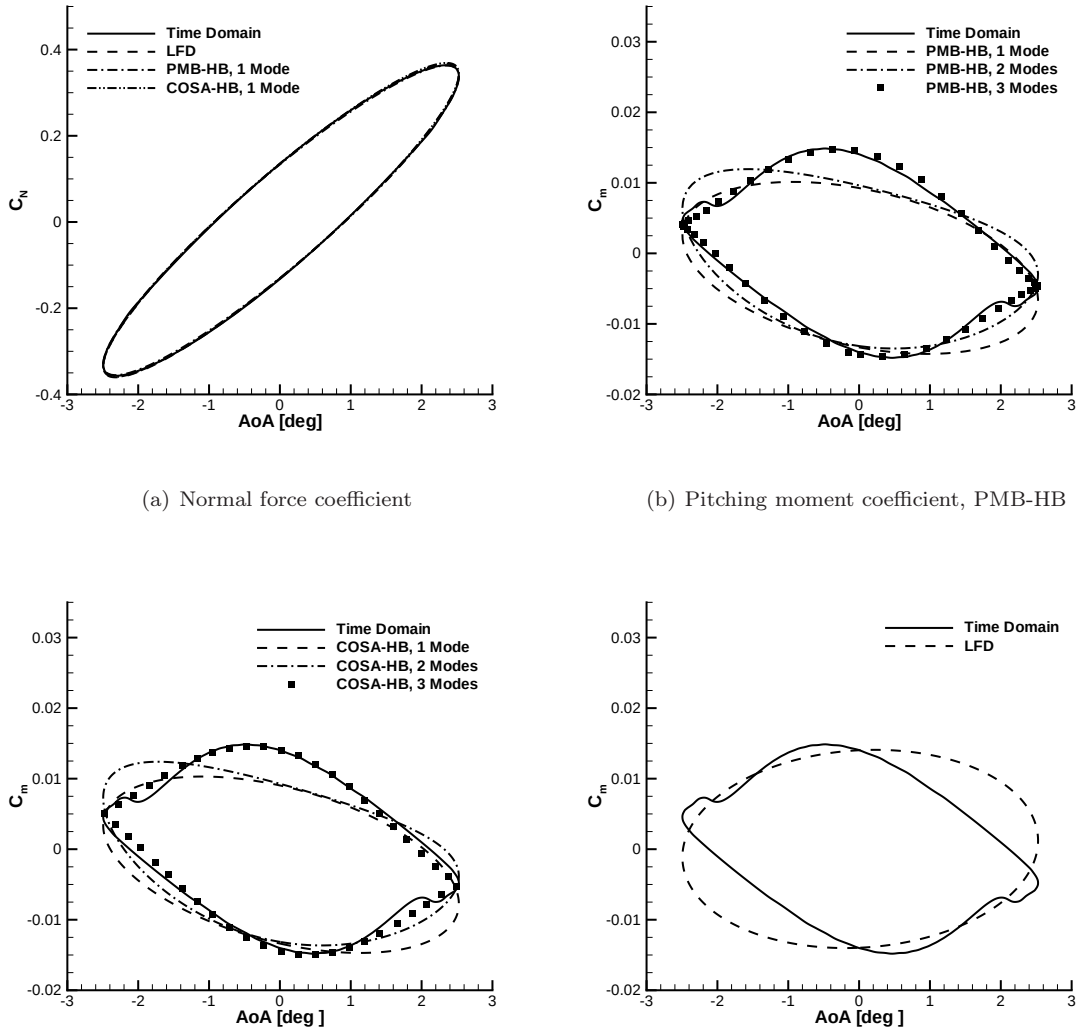

(a) Normal force coefficient

(b) Pitching moment coefficient, PMB-HB

(c) Pitching moment coefficient, COSA-HB

(d) Pitching moment coefficient, LFD

Fig. 5 NACA 0012: normal force and pitching moment coefficients dynamic dependence ($M = 0.755$, $\alpha_0 = 0.016$ deg, $\alpha_A = 2.51$ deg, and $k = 0.0814$)

Values from the one-mode HB and the LFD solutions are summarized in Table 3, along with the reference solution. In the table, the subscript and superscript indicate, respectively, the input

Table 3 NACA 0012: amplitude ratio and phase angle of the fundamental harmonic between the input, α, and the outputs, C_N and C_m

	$R_\alpha^{C_N}$	$\phi_\alpha^{C_N}$, [deg]	$R_\alpha^{C_m}$	$\phi_\alpha^{C_m}$, [deg]
Time Domain	0.144	-21.6	$4.80 \cdot 10^{-3}$	-112.1
PMB-HB, 1 Mode	0.143	-21.5	$4.86 \cdot 10^{-3}$	-112.1
COSA-HB, 1 Mode	0.145	-21.4	$4.98 \cdot 10^{-3}$	-116.3
LFD	0.145	-21.5	$5.60 \cdot 10^{-3}$	-85.2

and the output, and the phase angle is measured in degrees. Apart from the satisfactory agreement observed for the force data, a discrepancy is detected in the phase angle of the moment coefficient. For a sinusoidally varying input, a phase angle of -90 deg corresponds to shifting the response to a cosine function. The positive mean curve slope of the LFD solution in Fig. 5(d) reflects a phase lag in the moment dynamic dependence greater than -90 deg. On the contrary, a larger phase angle, in absolute value, reflects a negative mean curve slope, consistent with the one-mode HB solution.

To get further insights on the performance of the frequency-domain methods, the first harmonic unsteady surface pressure coefficient distribution is presented in Fig. 6. Results on the left side of the figure are for the one-mode HB and the LFD solutions, and the axis of rotation is also illustrated, while the right side illustrates the effect of retaining higher Fourier modes. Due to the similarity with the trends defined by the PMB-HB results, the COSA-HB solutions presented include only one Fourier mode. Figure 6(a) shows the zeroth harmonic, that is, the average value of the pressure coefficient through a cycle of unsteadiness. The HB solutions are identical for the two solvers, and are significantly different from the LFD solution. The asymmetric shock pattern on the lower and upper surfaces is attributable to the use of one Fourier mode and the actual location of the three time instances computed, which form a solution base sampled at uniformly spaced temporal intervals. Note that two snapshots feature a shock wave on the lower side, and on the upper surface for one snapshot, giving the over-prediction of the shock strength on the lower side and the under-prediction on the upper surface, in combination with a more upstream and downstream location, respectively. The mean solution of the LFD method corresponds to a steady-state analysis, and shows a good agreement away from the reference shock location. The

dynamic conditions of the prescribed forced motion moves the averaged shock position backward from its static position, determined at the mean angle of attack, by nearly twenty per cent of the aerofoil chord. Convergence to the time-accurate solution is obtained when increasing the number of modes in the HB method, as shown in Fig. 6(b). The real and imaginary parts, shown in Figs. 6(c) and 6(e), respectively, exhibit the already mentioned asymmetric pattern of the one-mode HB solution. Large spikes in the LFD solution are located around the steady-state shock position, and indicate a linear harmonic motion of the shock wave. The results for increasing number of harmonics are illustrated in Figs. 6(d) and 6(f). Note the different vertical scales used with respect to the prior set of corresponding figures. While consistently converging to the time-accurate solution, the rate of convergence is hindered by oscillations around the shock. Considering that three modes were adequate to approximate the moment dynamic dependence, this case illustrates the greater difficulty in converging a local quantity than an integrated one.

Table 4 summarizes the dynamic derivatives for the force and moment coefficients. A satisfactory agreement for the force dynamic derivatives is noted. For the moment values, the PMB-HB results illustrate that the one-mode solution provides a good estimation of the information needed for flight dynamics. The predictions of the LFD are reasonable for the aerodynamic damping term, while the in-phase component features a large inaccuracy. The contrasting sign reflects the observation that the moment loop was rotated in the opposite direction, indicating a longitudinal static instability. A consideration is that the steady-state shock wave, shown in Fig. 6(a), is located near the reference point at one quarter of the chord, and makes the moment data sensitive to any upstream or downstream variation of the resulting centre of pressure.

The frequency spectrum of the moment coefficient is presented in Fig. 7. Data for the time-domain solution are shown up to the seventh harmonic component. The LFD and the one-mode HB solutions show a good agreement for the magnitude term. The phase angle of the LFD solution differs by about thirty degrees from the HB counterpart. For the frequency range included, the amplitude of any odd harmonic is lower than the amplitude of the accompanying even harmonic. This arises from the symmetry of the aerofoil section and the nearly zero mean angle of attack.

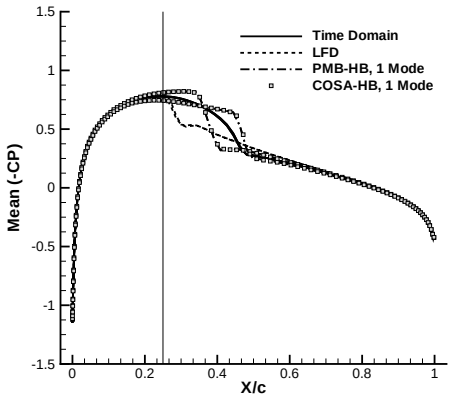

(a) Mean value

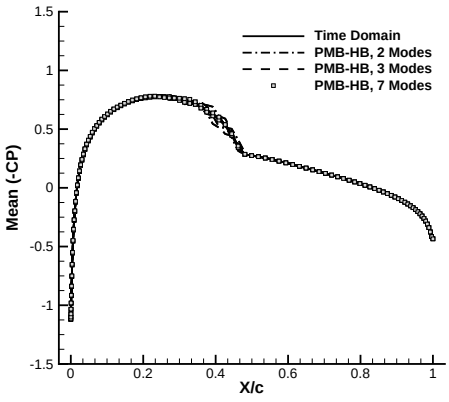

(b) Mean value, higher modes

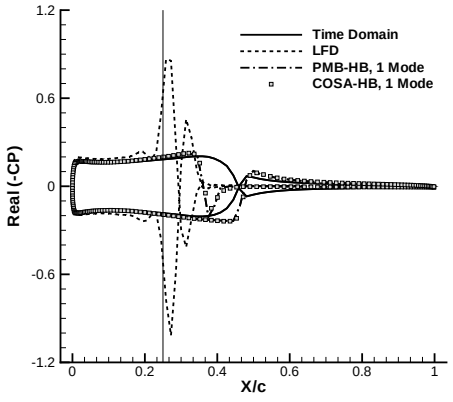

(c) Real part

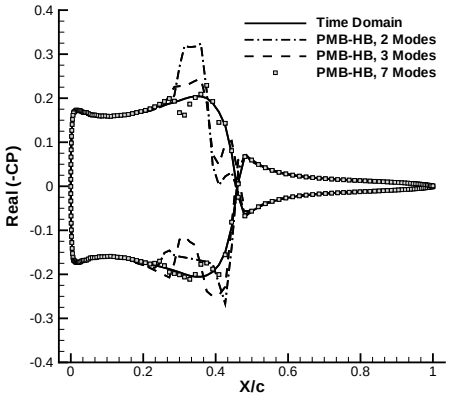

(d) Real part, higher modes

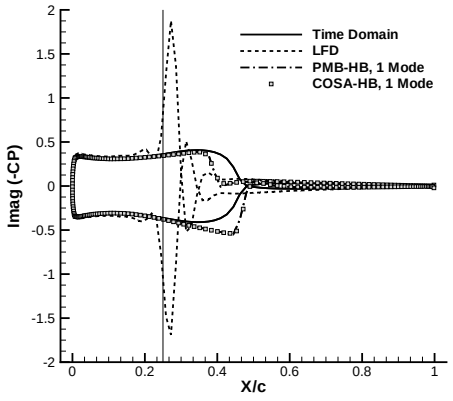

(e) Imaginary part

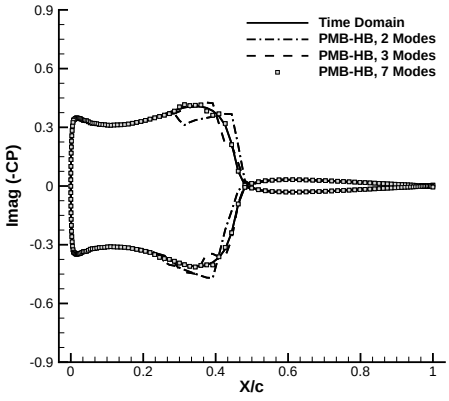

(f) Imaginary part, higher modes

Fig. 6 NACA 0012: zeroth and first harmonic unsteady surface pressure coefficient distribution ($M = 0.755$, $\alpha_0 = 0.016$ deg, $\alpha_A = 2.51$ deg, and $k = 0.0814$)

Table 4 NACA 0012: normal force and pitching moment coefficient dynamic derivatives ($M = 0.755$, $\alpha_0 = 0.016$ deg, $\alpha_A = 2.51$ deg, and $k = 0.0814$)

	$\bar{C}_{N_\alpha}$	$\bar{C}_{N_q}$	$\bar{C}_{m_\alpha}$	$\bar{C}_{m_q}$
Time Domain	7.66	$-3.72 \cdot 10^{1}$	$-1.03 \cdot 10^{-1}$	-3.14
PMB-HB, 1 Mode	7.63	$-3.70 \cdot 10^{1}$	$-1.04 \cdot 10^{-1}$	-3.17
PMB-HB, 2 Modes	7.63	$-3.72 \cdot 10^{1}$	$-1.06 \cdot 10^{-1}$	-3.19
PMB-HB, 3 Modes	7.64	$-3.72 \cdot 10^{1}$	$-1.02 \cdot 10^{-1}$	-3.14
PMB-HB, 4 Modes	7.65	$-3.72 \cdot 10^{1}$	$-1.04 \cdot 10^{-1}$	-3.15
PMB-HB, 5 Modes	7.65	$-3.72 \cdot 10^{1}$	$-1.03 \cdot 10^{-1}$	-3.14
PMB-HB, 6 Modes	7.65	$-3.72 \cdot 10^{1}$	$-1.03 \cdot 10^{-1}$	-3.14
PMB-HB, 7 Modes	7.65	$-3.72 \cdot 10^{1}$	$-1.03 \cdot 10^{-1}$	-3.14
LFD	7.73	$-3.73 \cdot 10^{1}$	$0.27 \cdot 10^{-1}$	-3.93

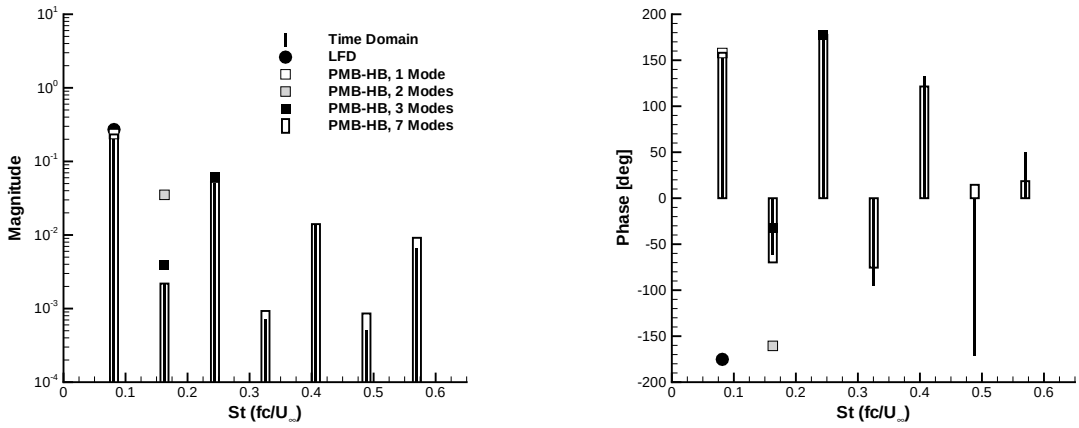

(a) Magnitude

(b) Phase

Fig. 7 NACA 0012: magnitude and phase of pitching moment coefficient ($M = 0.755$, $\alpha_0 = 0.016$ deg, $\alpha_A = 2.51$ deg, and $k = 0.0814$)

D. Computational Efficiency

Figure 8 conveys the computational efficiency of the spectral methods with respect to the underlying time-domain simulation. For the comparison, the solutions were obtained using 128 time-steps per cycle and were simulated for 3 periods. In this case, the LFD solution was obtained in about 5% of the time of the corresponding time-domain solver. While achieving the largest computational

saving time, a loss in accuracy was observed in the LFD-based predictions of dynamic derivatives. With a performance similar to the LFD solver, the HB formulation was seen to be adequate for the prediction of stability characteristics and local flow variables. By retaining more Fourier modes, the HB method rapidly loses favor relative to solving the time-dependent equations. The computational efficiency of the HB method depends on the numerical integration method. Using an explicit integration strategy like the multigrid iteration implemented by COSA, the computational cost for solving the HB equations grows linearly with the number of harmonics. This is because the convergence rate of the multigrid solver is fairly independent of the number of harmonics and the cost of each multigrid iteration is proportional to the number of harmonics. In the case of the fully implicit integration of the HB equations implemented in the PMB code, conversely, the computational cost associated with each iteration required to solve the linear system arising at each step of the implicit integration is proportional to the square of the number of harmonics. Since the overall number of linear iterations for solving the HB equations does not vary significantly with the number of harmonics, the overall solution cost is proportional to the square of the number of harmonics. These considerations explain why the COSA-HB solver becomes more efficient than the PMB-HB solver when more than two harmonics are used.

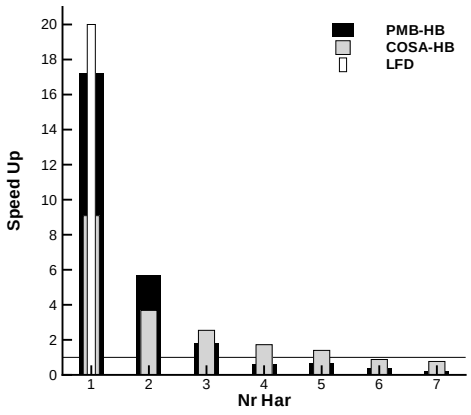

Fig. 8 NACA 0012: CPU time speed up of the frequency-domain methods with respect to the underlying time-domain method

A detailed quantification of the computational efficiency of the HB method compared with the

underlying unsteady solution was undertaken for the PMB solver pair, and following the procedure outlined in reference [44]. To assess the sensitivity of the temporal discretization used, unsteady solutions were obtained using 8, 16, 32, 64, 128, 256, 512 and 1024 time-steps per oscillatory cycle. All cases were run using the same solver parameters. To reduce the effects of the initial transient on the solution, eleven cycles were simulated. The damping-in-pitch term was taken as the figure of merit, which is of interest for this work. For each run, the dynamic term was determined from the last cycle of the solution computed, and compared with the reference value obtained from the most accurate simulation, that is, using 1024 time-steps. The norm

$$E_n \;=\; |\bar{C}^{n}_{m_q} - \bar{C}^{1024}_{m_q}| \,/\, |\bar{C}^{1024}_{m_q}| \tag{24}$$

indicates the temporal error. The procedure was also adopted for the PMB-HB results, and the seven-mode solution was assumed the reference solution. Figure 9(a) shows the error levels for the two solvers. The intersection of the PMB-HB lines with the PMB curve indicates the temporal resolution needed in the unsteady simulation to achieve an equivalent error level. To match the error level defined by the one-mode PMB-HB solution, 50 time-steps per oscillation are required for the time-domain simulation, increasing to 90 to guarantee a similar error level as for the three-mode HB solution. A convergence study was then performed to identify the number of oscillatory cycles needed to obtain asymptotic convergence. Results for the two time-steps are shown in Fig. 9(b). The curves converge to an error level representing the minimum error achievable using the corresponding time-step size. Convergence is observed after 3 oscillatory cycles for the larger time-step size, increasing to 6 in combination with the finer step increment. Data are summarized in Table 5. It was found that the execution time of the HB solution using one-mode is about 11 times faster than the time required for the unsteady results. The time saving decreases to less than 3 times when three-modes are retained in the solution. Increased work associated with the linear solver as the number of modes is increased contributes to increased cost.

IV. Three-Dimensional Case

The second test case is for a civil passenger transport aircraft tested at the German Aerospace Center (DLR), and referred to as the DLR-F12 model. Extensive tunnel investigations and nu-

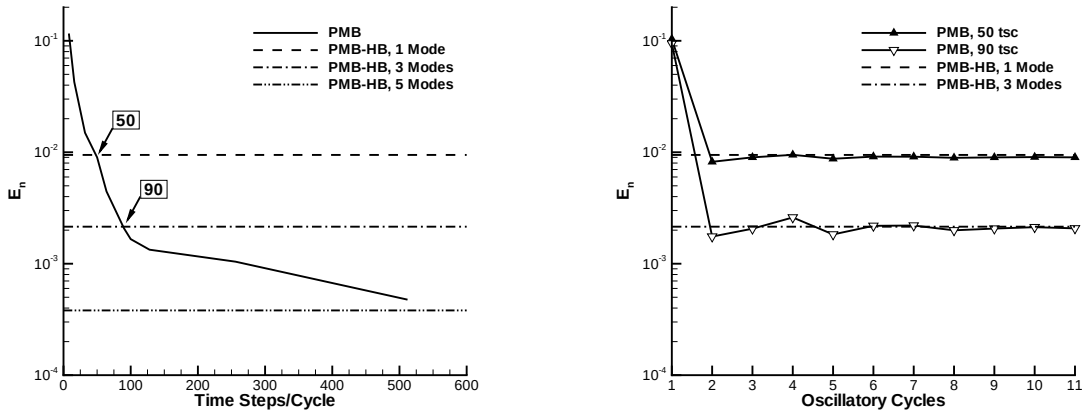

(a) Estimating the number of time-steps per cycle

(b) Estimating the number of cycles

Fig. 9 NACA 0012: error norm in the prediction of the damping-in-pitch obtained using the PMB solver pair; in (b), the term tsc indicates the number of time steps per cycle

Table 5 NACA 0012: time reduction of the PMB-HB solution compared to unsteady PMB solution using the damping-in-pitch as the figure of merit; the terms tsc and n_c indicate, respectively, the number of time-steps per cycle and the number of oscillatory cycles

PMB-HB	PMB	Speed-Up
	$(tsc \times n_c)$	
1 Mode	50×3	10.9
3 Modes	90×6	2.6

merical simulations were made for low speeds and low angles of attack [39, 45–48]. The emphasis in the current work is for a transonic cruise condition, which has been investigated in a previous work [49] using the Euler and Reynolds-averaged Navier-Stokes equations. Given the large number of investigations focussed on linear aerodynamics, it is disappointing that only the study detailed in reference [49] looked at flow regimes of interest for a transport configuration.

A. Numerical Setup

Two Euler grids for the half-configuration of the wind tunnel model were used for the PMB and TAU pairs, shown in Fig. 10. A structured grid including 300 blocks was generated with around 2 million grid points, and 1.8 million points were used for the unstructured grid. A detailed comparison

Table 6 Description of the conditions for the DLR-F12 aircraft model

Parameter	Value
M	0.73
α_0	0.70 deg
α_A	0.50 deg
k	0.034
h	6000 m

of the structured and unstructured grids can be found, for example, in Mialon et al. [46].

Calculations presented in this paper are for a cruise condition at an altitude of 6000 m, Mach number of 0.73 and trim angle of attack of 0.7 deg. The analysis is performed on the clean configuration with undeflected control surfaces. This was considered a reasonable simplification because the required trim elevator deflection is lower than one degree and, consistent with the traditional mathematical formulation, forces and moments are expanded in a Taylor series around the equilibrium level flight condition to obtain the stability and control derivatives. Data for the oscillatory pitching motion are summarized in Table 6. The mean aerodynamic chord of the wind tunnel model is $c = 0.2526$ m. The rotation point and the model centre of gravity are coincident and located at 46.7% of the fuselage length from the foremost point. The moment reference point is set at the aircraft nose.

Unsteady simulations were run for three periods using 128 time-steps per cycle. Note that all time-domain calculations were repeated for a smaller time-step that has twice the number of points per cycle, with identical results obtained. For the TAU solver, a GMRES Krylov solver was used in combination with a "3v" multigrid cycle as preconditioner at a CFL number of 10. The PMB calculations were also run at a constant CFL number of 10. The HB method was run with one Fourier mode only. The COSA solver was not run for the current configuration.

B. Results

Results obtained using the PMB and TAU solvers are illustrated in Fig. 11. Aerodynamic loops are similar in shape, and in this case the shock motion does not introduce a large distortion from

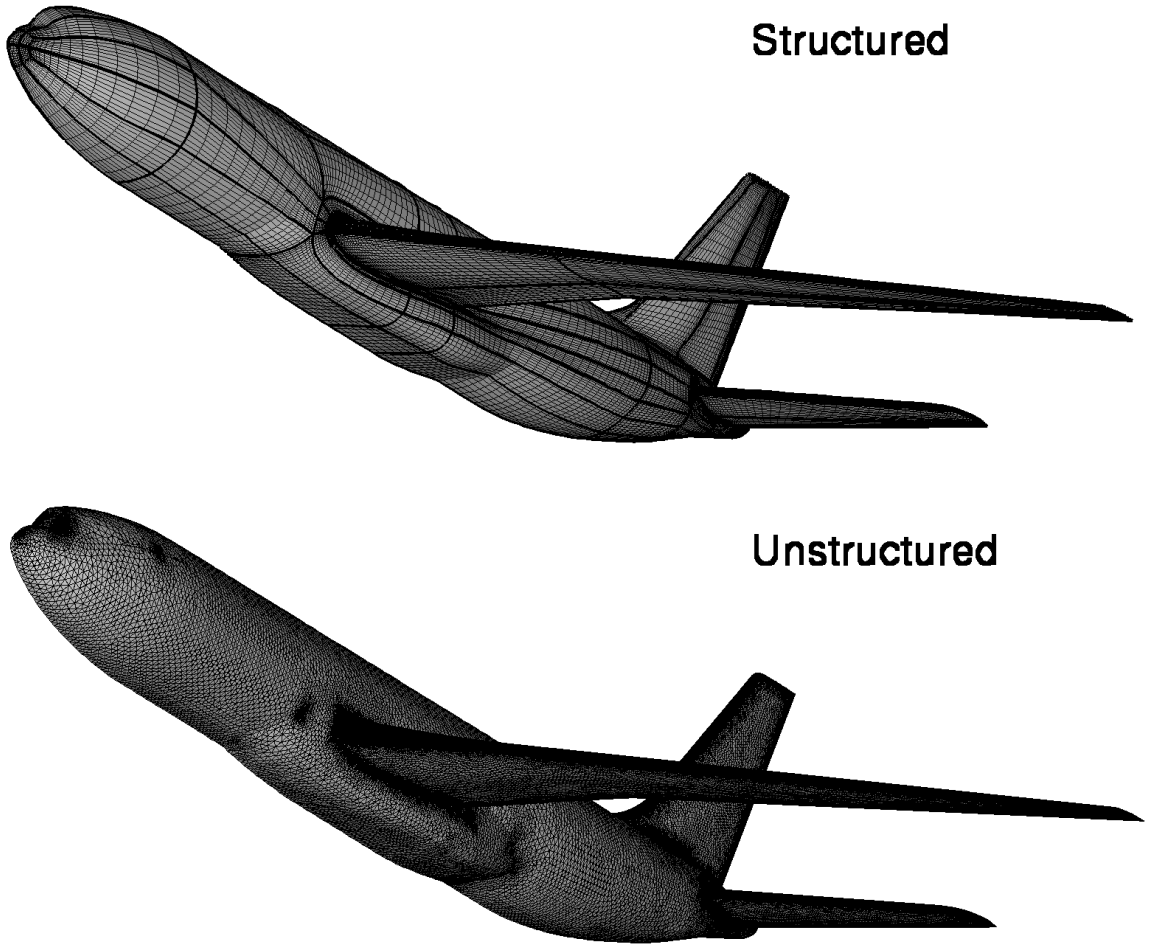

Fig. 10 Structured and unstructured grids for the DLR-F12 model

a harmonic time response, when compared with the aerofoil case. For the pitching moment, the contribution from the dynamic derivative is negative, and the slope is also negative. This guarantees that the aircraft is statically and dynamically stable in the longitudinal plane. When comparing Figs. 11(b) and 11(d), a deviation in the values of the pitching moment at the lower end of the angle of attack range can be detected, indicating some grid dependence in the solutions.

Frequency-domain calculations are illustrated for comparison to the underlying CFD solver in Fig. 11. It is observed that the HB solution reproduces the force and moment dynamic dependence well, whereas the LFD solution underpredicts the hysteresis in the moment data. As shown below, this deficiency of the LFD is attributable to underpredicting the real part of the first harmonic pressure coefficient distribution on the horizontal tail.

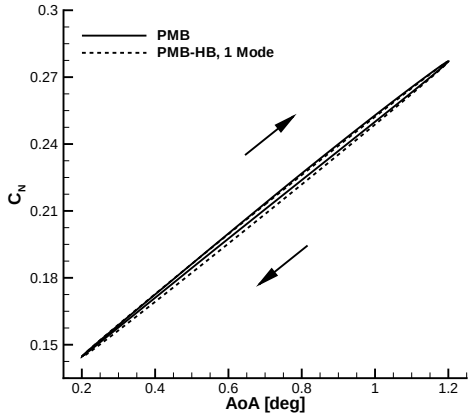

(a) Normal force coefficient, PMB-HB

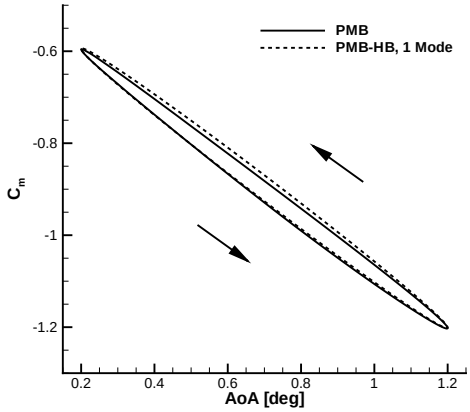

(b) Pitching moment coefficient, PMB-HB

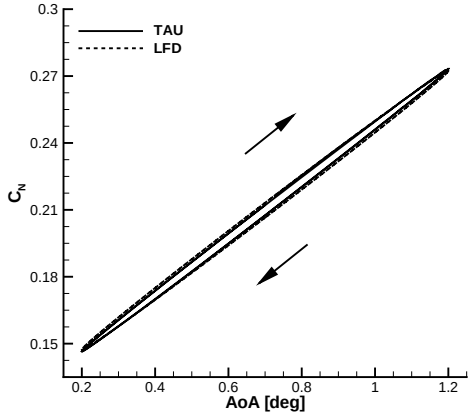

(c) Normal force coefficient, LFD

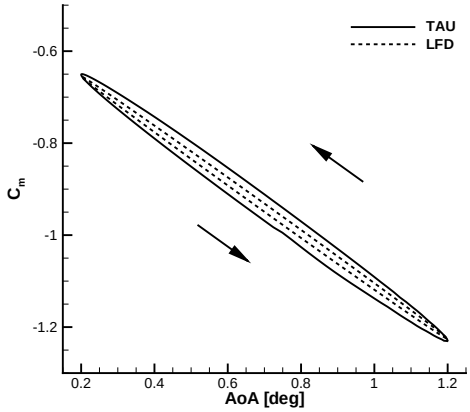

(d) Pitching moment coefficient, LFD

Fig. 11 DLR-F12 model: normal force and pitching moment coefficients dynamic dependence ($M = 0.73$, $\alpha_0 = 0.70$ deg, $\alpha_A = 0.50$ deg, $k = 0.034$, and $h = 6000$ m)

Stability characteristics relative to the nominal flight conditions are summarized in Table 7, which includes static and dynamic derivatives. Frequency-domain results are in agreement with the respective time-domain results, with the exception of the LFD method in the prediction of the damping-in-pitch term. However, the HB solution performs well, with deviations within 7% of the PMB time-domain values. A consideration is that the reduction of the hysteresis in the aerodynamic loads for relatively small values of the reduced frequency leads to a difficulty in the accurate prediction of the damping terms because of a reduction in the aerodynamic load increments. This poses significant practical challenges for wind-tunnel testing and for numerical simulations [14,

Table 7 DLR-F12 model: normal force and pitching moment coefficient dynamic derivatives ($M = 0.73$, $\alpha_0 = 0.70$ deg, $\alpha_A = 0.50$ deg, $k = 0.034$, and $h = 6000$ m)

	$C_{N\,0}$	$\bar{C}_{N_\alpha}$	$\bar{C}_{N_q}$	$C_{m\,0}$	$\bar{C}_{m_\alpha}$	$\bar{C}_{m_q}$
PMB	$2.11\cdot 10^{-1}$	7.59	1.17	$-9.00\cdot 10^{-1}$	-34.7	-20.1
PMB-HB, 1 Mode	$2.11\cdot 10^{-1}$	7.60	1.65	$-8.99\cdot 10^{-1}$	-34.7	-21.6
TAU	$2.10\cdot 10^{-1}$	7.16	2.80	$-9.41\cdot 10^{-1}$	-32.7	-28.1
LFD	$2.10\cdot 10^{-1}$	7.26	3.28	$-9.41\cdot 10^{-1}$	-33.1	-17.7

45]. Also note that differences in the force data computed by time-domain solvers are amplified in calculating dynamic derivatives by a factor $1/k$, where for this test case $k = 0.034$. While reducing substantially the computational cost compared to a time-accurate solution, one single calculation with a frequency-domain method provides both static and dynamic derivative information. In this case, the frequency-domain solutions based on the HB and LFD methods were obtained in approximately 3% of the time required for a time-accurate simulation. This corresponds to a speed up of about 30. Due to the computational cost of the time-accurate method, an objective evaluation of the computational efficiency of the frequency-domain methods, similar to that outlined for the aerofoil case, was not performed.

Again, the zeroth and first harmonic of the pressure coefficient distribution at a spanwise section $Y/s = 0.148$ is shown in detail in Fig. 12. The selected spanwise section intersects both wing and horizontal tail, and features a periodically moving shock wave on the wing. The left and right side of the figure illustrates, respectively, the wing and horizontal tail station. The steady-state solution based on the LFD solver and the time-averaged solution are in good agreement, as seen in Figs. 12(a) and 12(b). This is indicative of less significant dynamic effects due to the limited oscillatory amplitude. Two considerations are noted for the real part of the first harmonic, shown in Figs. 12(c) and 12(d). The contribution from the wing is much smaller than the contribution which originates from the horizontal tail. This is expected because of the finite time to convect downstream changes in aircraft attitude. On the horizontal tail, a difference between time-accurate solutions occurs around the suction peak, where the formation of a shock wave of limited extent was observed during part of the sinusoidal cycle. At this section, the LFD solution differs substantially

from the reference solution, and this causes the underprediction of the hysteresis in the moment loop observed in Fig. 11(d). This shows the limitations of the LFD method in cases featuring dynamic non-linearities not present in the steady-state reference solution. A better correlation of the frequency-domain methods to the underlying method is observed for the imaginary part. As expected, the response on the wing is larger in this case when compared to the real part of the pressure distribution.

V. Conclusions

The current work explored the capabilities and limitations of the Harmonic Balance and Linear Frequency Domain methods in predicting aircraft stability characteristics in a computationally efficient way. Two test cases were presented, a NACA 0012 aerofoil and a wind tunnel aircraft configuration based on the DLR-F12 wind tunnel model. To stress the potential of the frequency-domain methods in conditions of practical interest for aircraft applications, flow conditions were in the transonic regime. For the formation of moving shock waves, the energy of aerodynamic modes redistribute at higher frequencies than the predescribed frequency of motion. While a time-domain calculation supports a continuum of frequencies up to the frequency limits given by the temporal and spatial resolution, the Harmonic Balance and Linear Frequency Domain methods resolve only a small subset of frequencies typically restricted to include one Fourier mode at the frequency at which dynamic derivatives are desired.

For the aerofoil case, it was noted that the Harmonic Balance method was able to predict dynamic derivatives very accurately. For the Linear Frequency Domain method, a loss in accuracy may be experienced whenever amplitudes increase and moving shocks appear. In terms of pressure distribution, convergence to time-accurate results was assessed for an increasing number of Fourier modes in the Harmonic Balance solution. It was demonstrated that the dynamic conditions of the prescribed forced motion moves the average shock position downstream from its static position by nearly twenty per cent of the aerofoil chord. In this case, a loss in accuracy of the Linear Frequency Domain method is expected. Numerical experiments for these cases demonstrate that the Harmonic Balance and Linear Frequency Domain methods are an order of magnitude more efficient than

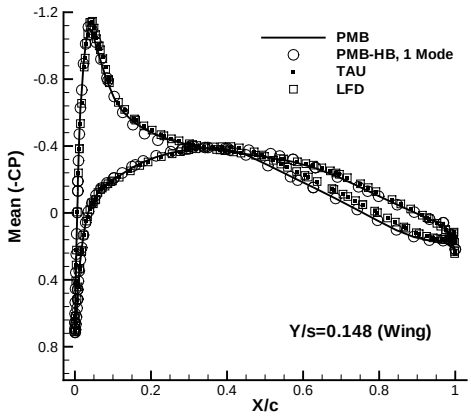

(a) Mean value (wing)

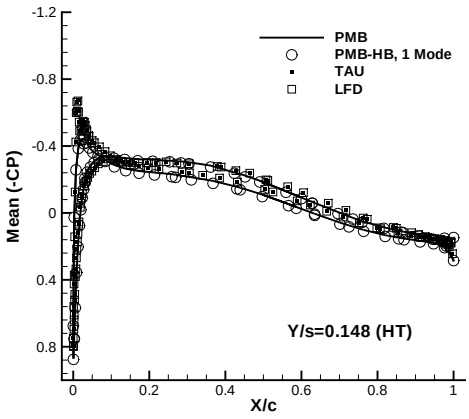

(b) Mean value (horizontal tail)

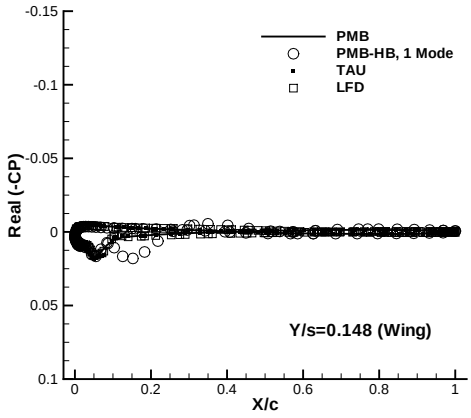

(c) Real part (wing)

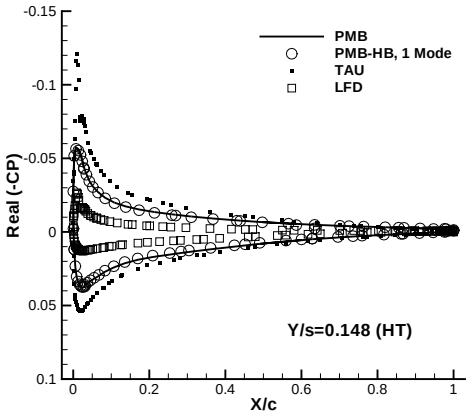

(d) Real part (horizontal tail)

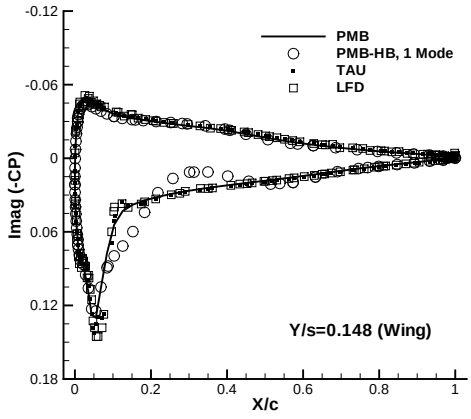

(e) Imaginary part (wing)

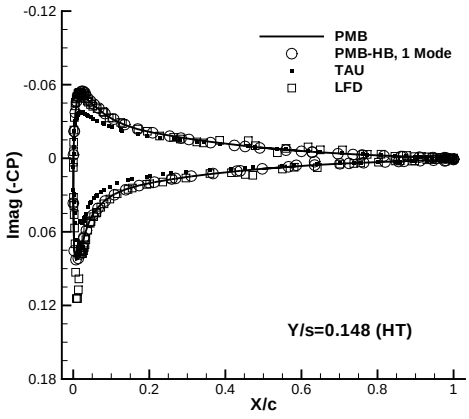

(f) Imaginary part (horizontal tail)

Fig. 12 DLR-F12 model: zeroth and first harmonic unsteady surface pressure coefficient distribution at $Y/s = 0.148$ ($M = 0.73$, $\alpha_0 = 0.70$ deg, $\alpha_A = 0.50$ deg, $k = 0.034$, and $h = 6000$ m)

time-accurate methods.

Similar considerations were noted for a three-dimensional configuration based on the DLR-F12 wind tunnel model, for which a comparison of static and dynamic stability derivatives was presented. One single calculation with a frequency-domain method provides both static and dynamic derivative information at a fraction of the calculation time of a time-accurate simulation. In this case, the cost of the frequency-domain method was approximately 3% of the unsteady counterpart.

VI. Acknowledgements

The work at Liverpool was supported by the SimSAC project under funding from the Sixth Framework programme of the European Union, the Engineering and Physical Sciences Research Council and the Ministry of Defence under EP/D504473/1, the ECERTA project under funding from the Sixth Framework Marie Curie Excellence Team, and an Airbus PhD studentship. The work at Glasgow was supported by the Engineering and Physical Sciences Research Council under grant EP/F038542/1.

References

[1] Bryan, G. H., *Stability in Aviation*, MacMillan, London, 1911.

[2] Pamadi, N. B., *Performance, Stability, Dynamics, and Control of Airplanes*, AIAA Education Series, American Institute of Aeronautics and Astronautics, Inc., Reston, Virginia, USA, 2nd ed., 2004.

[3] Kimberlin, R. D., *Flight Testing of Fixed-Wing Aircraft*, AIAA Education Series, American Institute of Aeronautics and Astronautics, Inc., Reston, Virginia, USA, 2003.

[4] Barlow, J. B., William, H. R., and Pope, A., *Low-Speed Wind Tunnel Testing*, John Wiley & Sons, Inc., 3rd ed., 1999.

[5] Williams, J. E. and Vukelich, S. R., "The USAF Stability and Control Digital DATCOM," 63166, 1979, AFFDL-TR-79-3032.

[6] Raymer, D. P., *Aircraft Design: A Conceptual Approach*, AIAA Education Series, American Institute of Aeronautics and Astronautics, Inc., Reston, Virginia, USA, 4th ed., 2006.

[7] Boelens, O. J., Badcock, K. J., Elmilgui, A., Abdol-Hamid, K. S., and Massay, S. J., "Comparison of Measured and Block Structured Simulation Results for the F-16XL Aircraft," *Journal of Aircraft*, Vol. 46, No. 2, 2009, pp. 377–384, doi: 10.2514/1.35064.

[8] McDaniel, D. R., Cummings, R. M., Bergeron, K., Morton, S. A., and Dean, J. P., "Comparisons of Computational Fluid Dynamics Solutions of Static and Manoeuvring Fighter Aircraft with Flight Test Data," Proceedings of the Institution of Mechanical Engineers, Part G: Journal of Aerospace Engineering, 2009, doi: 10.1243/09544100JAERO411.

[9] Da Ronch, A., Ghoreyshi, M., and Badcock, K. J., "On the Generation of Flight Dynamics Aerodynamic Tables by Computational Fluid Dynamics," *Progress in Aerospace Sciences*, Vol. 47, No. 8, 2011, pp. 597–620, doi: 10.1016/j.paerosci.2011.09.001.

[10] Da Ronch, A., McFarlane, C., Beaverstock, C., Oppelstrup, J., Zhang, M., and Rizzi, A., "Benchmarking CEASIOM Software to Predict Flight Control and Flying Qualities of the B–747," *Proceedings of the 27th Congress of the International Council of the Aeronautical Sciences*, ICAS Paper 2010–282, 2010.

[11] Richardson, T., McFarlane, C., Isikveren, A., Badcock, K. J., and Da Ronch, A., "Analysis of Conventional and Asymmetric Aircraft Configurations Using CEASIOM," *Progress in Aerospace Sciences*, Vol. 47, No. 8, 2011, pp. 647–659, doi: 10.1016/j.paerosci.2011.08.008.

[12] Richardson, T., Beaverstock, C., Isikveren, A., Meheri, A., Badcock, K. J., and Da Ronch, A., "Analysis of the Boeing 747-100 Using CEASIOM," *Progress in Aerospace Sciences*, Vol. 47, No. 8, 2011, pp. 695–705, doi: 10.1016/j.paerosci.2011.08.009.

[13] Da Ronch, A., Vallespin, D., Ghoreyshi, M., and Badcock, K. J., "Evaluation of Dynamic Derivatives Using Computational Fluid Dynamics," *AIAA Journal*, Vol. 50, No. 2, 2012, pp. 470–484, doi: 10.2514/1.J051304.

[14] Thompson, J. R., Frink, N. T., and Murphy, P. C., "Guidelines for Computing Longitudinal Dynamic Stability Characteristics of a Subsonic Transport," *28th AIAA Applied Aerodynamic Conference*, AIAA–2010–4819, 2010.

[15] Clark, W. S. and Hall, K. C., "A Time-Linearized Navier-Stokes Analysis of Stall Flutter," *Journal of Turbomachinery*, Vol. 122, No. 3, 2000, pp. 467–476, doi: 10.1115/1.1303073.

[16] van der Weide, E., Gopinath, A. K., and Jameson, A., "Turbomachinery Applications with the Time Spectral Method," *35th AIAA Fluid Dynamics Conference and Exhibit*, AIAA Paper 2005–4905, 2005.

[17] Blanc, F., Roux, F. X., and Jouhaud, J. C., "Harmonic-Balance-Based Code-Coupling Algorithm for Aeroelastic Systems Subjected to Forced Excitation," *AIAA Journal*, Vol. 48, No. 11, 2010, pp. 2472–2481, doi: 10.2514/1.45444.

[18] Pechloff, A. and Laschka, B., "Small Disturbance Navier-Stokes Computations for Low-Aspect-Ratio Wing Pitching Oscillations," *Journal of Aircraft*, Vol. 47, No. 3, 2010, pp. 737–753, doi: 10.2514/1.45233.

[19] Dufour, G., Sicot, F., and Puigt, G., "Contrasting the Harmonic Balance and Linearized Methods for Oscillating–Flap Simulations," *AIAA Journal*, Vol. 48, No. 4, April 2010, doi: 10.2514/1.43401.

[20] Murman, S. M., "Reduced-Frequency Approach for Calculating Dynamic Derivatives," *AIAA Journal*, Vol. 45, No. 6, 2007, pp. 1161–1168, doi: 10.2514/1.15758.

[21] Maple, R. C., King, P. I., and Oxley, M. E., "Adaptive Harmonic Balance Solutions to Euler's Equation," *AIAA Journal*, Vol. 41, No. 9, 2003, pp. 1705–1714, doi: 10.2514/2.7316.

[22] Maple, R. C., King, P. I., Orkwis, P. D., and Wolff, J. M., "Adaptive Harmonic Balance Method for Nonlinear Time-Periodic Flows," *Journal of Computational Physics*, Vol. 193, No. 2, 2004, pp. 620–641, doi: 10.1016/j.jcp.2003.08.013.

[23] McCracken, A., Da Ronch, A., and Badcock, K. J., "Requirements for Computer Generated Aerodynamic Models for Aircraft Stability and Control Analysis," *5th Symposium on Integrating CFD and Experiments in Aerodynamics*, Tokyo, Japan, 3-5 Oct., 2012.

[24] Badcock, K. J., Richards, B. E., and Woodgate, M. A., "Elements of Computational Fluid Dynamics on Block Structured Grids using Implicit Solvers," *Progress in Aerospace Sciences*, Vol. 36, 2000, pp. 351–392, doi: 10.1016/S0376-0421(00)00005-1.

[25] Osher, S. and Chakravarthy, S., "Upwind Schemes and Boundary Conditions with Applications to Euler Equations in General Geometries," *Journal of Computational Physics*, Vol. 50, No. 3, 1983, pp. 447–481, doi: 10.1016/0021-9991(83)90106-7.

[26] Van Leer, B., "Towards the Ultimate Conservative Difference Scheme II: Monotonicity and Conservation Combined in a Second Order Scheme," *Journal of Computational Physics*, Vol. 14, No. 4, 1974, pp. 361–374, doi: 10.1016/0021-9991(74)90019-9.

[27] Jameson, A., "Time Dependent Calculations Using Multigrid, with Applications to unsteady Flows Past Airfoils and Wings," AIAA Paper 91–1596, 1991.

[28] Gerhold, T., Galle, M., Friedrich, O., and Evans, J., "Calculation of Complex Three-Dimensional Configurations employing the DLR TAU-Code," AIAA Paper 97-0167, 1997.

[29] Schwamborn, D., Gerhold, T., and Heinrich, R., "The DLR TAU-Code: Recent Applications in Research and Industry," *Proceedings of European Conference on Computational Fluid Dynamics ECCOMAS CFD*, 2006.

[30] Dwight, R., Brezillon, J., and Vollmer, D., "Efficient Algorithms for Solution of the Adjoint Compressible Navier-Stokes Equations with Applications," *Proceedings of the ONERA-DLR Aerospace Symposium (ODAS), Toulouse*, 2006.

[31] Campobasso, M. S., Bonfiglioli, A., and Baba-Ahmadi, M. H., "Development of Efficient and Accu-

rate CFD Technologies for Wind Turbine Unsteady Aerodynamics," *Proceedings of the Conference on Modeling Fluid Flow*, Vol. 2, 2009, pp. 879–886.

[32] Bonfiglioli, A., Campobasso, M. S., and Carpentieri, B., "Parallel Unstructured Three-Dimensional Turbulent Flow Analyses Using Efficiently Preconditioned Newton-Krylov Solver," *19th AIAA Computational Fluid Dynamics Conference*, AIAA Paper 2009-4137, 2009.

[33] Campobasso, M. S. and Baba-Ahmadi, M. H., "Ad-hoc Boundary Conditions for CFD Analyses of Turbomachinery Problems with Strong Flow Gradients at Farfield Boundaries," *ASME Journal of Turbomachinery*, Vol. 133, No. 4, 2011, doi: 10.1115/1.4002985.

[34] Hall, K. Thomas, J. and Clark, W., "Computation of Unsteady Nonlinear Flows in Cascades Using a Harmonic Balance Technique," *AIAA Journal*, Vol. 40, No. 5, May, 2002, pp. 879–886, doi: 10.2514/2.1754.

[35] Woodgate, M. and Badcock, K., "Implicit Harmonic Balance Solver for Forced Motion Transonic Flow," *AIAA Journal*, Vol. 47, No. 4, 2008, pp. 893–901, doi: 10.2514/1.36311.

[36] Campobasso, M. S. and Baba-Ahmadi, M. H., "Analysis of Unsteady Flows Past Horizontal Axis Wind Turbine Airfoils Based on Harmonic Balance Compressible Navier-Stokes Equations with Low-Speed Preconditioning," ASME Paper GT2011–45303, 2011.

[37] Thomas, J. P., Duster, C. H., Dowell, E. H., and Hall, K. C., "Unsteady Flow Computation Using a Harmonic Balance Approach Implemented About the OVERFLOW 2 Flow Solver," *19th AIAA Computational Fluid Dynamics Conference*, AIAA Paper 2009–4270, 2009.

[38] Jackson, A., Campobasso, M. S., and Baba-Ahmadi, M. H., "On the Parallelization of a Harmonic Balance Compressible Navier-Stokes Solver for Wind Turbine Aerodynamics," ASME paper GT2011–45306, 2011.

[39] Widhalm, M., Dwight, R. P., Thormann, R., and Hübner, A. R., "Efficient Computation of Dynamic Stability Data with a Linearized Frequency Domain Solver," *Proceedings of European Conference on Computational Fluid Dynamics ECCOMAS CFD*, 2010.

[40] Landon, R. H., "NACA 0012. Oscillating and Transient Pitching," In Compendium of Unsteady Aerodynamic Measurements, AGARD-R-702, Data Set 3, August 1982.

[41] Green, L. L. and Newman, P. A., "Wall-Interference Assessment and Corrections for Transonic NACA 0012 Airfoil Data from Various Wind Tunnels," NASA Technical Paper 3070, April, 1991.

[42] Batina, J. T., "Unsteady Euler Airfoil Solutions Using Unstructured Dynamic Meshes," *AIAA Journal*, Vol. 28, No. 8, 1990, pp. 1381–1388, doi: 10.2514/3.25229.

[43] Marques, A. N., Simões, C. F. C., and Azevedo, J. L. F., "Unsteady Aerodynamic Forces for Aeroelastic

Analysis of Two-Dimensional Lifting Surfaces," *Journal of the Brazilian Society of Mechanical Sciences and Engineering*, Vol. 28, No. 4, 2006, pp. 474–484, doi: 10.1590/S1678-58782006000400013.

[44] McMullen, M. S., *The Application of Non-Linear Frequency Domain Methods to the Euler and Navier-Stokes Equations*, Ph.D. thesis, Stanford University, Stanford, CA, USA, March 2003.

[45] Da Ronch, A., Ghoreyshi, M., Badcock, K. J., Görtz, S., Widhalm, M., Dwight, R. P., and Campobasso, M. S., "Linear Frequency Domain and Harmonic Balance Predictions of Dynamic Derivatives," *28th AIAA Applied Aerodynamic Conference*, AIAA Paper 2010–4699, 2010.

[46] Mialon, B., Khelil, S. B., Huebner, A., Jouhaud, J.-C., Rogé, G., Hitzel, S., Badcock, K., Eliasson, P., Khrabov, A., and Lahuta, M., "European Benchmark on Numerical Prediction of Stability and Control Derivatives," *27th AIAA Applied Aerodynamics Conference*, AIAA Paper 2009–4116, 2009.

[47] Hübner, A. R., Bergmann, A., and Löser, T., "Experimental and Numerical Investigations of Unsteady Force and Pressure Distributions of Moving Transport Aircraft Configurations," *47th AIAA Aerospace Sciences Meeting*, AIAA–2009–0091, 2009.

[48] Mialon, B., Khrabrov, A., Khelil, S. B., Huebner, A., Da Ronch, A., Badcock, K. J., Cavagna, L., Eliasson, P., Zhang, M., Ricci, S., Jouhaud, J.-C., Rogé, G., Hitzel, S., and Lahuta, M., "Validation of Numerical Prediction of Dynamic Derivatives: The DLR-F12 and the Transcruiser Test Cases," *Progress in Aerospace Sciences*, Vol. 47, No. 8, 2011, pp. 674–694, doi: 10.1016/j.paerosci.2011.08.010180.

[49] Ghoreyshi, M., Badcock, K. J., Da Ronch, A., Vallespin, D., and Rizzi, A., "Automated CFD Analysis for the Investigation of Flight Handling Qualities," *Mathematical Modelling of Natural Phenomena*, Vol. 6, No. 3, 2011, doi: 10.1051/mmnp/20116307.